

# Direct observations of L-I-H and H-I-L transitions with the X-point reciprocating probe in ASDEX Upgrade

S.H. Müller,<sup>1</sup> G.D. Conway,<sup>2</sup> G. Birkenmeier,<sup>2</sup> D. Carralero,<sup>2</sup> T. Happel,<sup>2</sup> A. Herrmann,<sup>2</sup> P. Manz,<sup>3,2</sup> P. de Marné,<sup>2</sup> A. Mlynek,<sup>2</sup> H.W. Müller,<sup>2</sup> S. Potzel,<sup>2</sup> V. Rohde,<sup>2</sup> U. Stroth,<sup>2,3</sup> M. Tsalas,<sup>4</sup> G.R. Tynan,<sup>1</sup> E. Wolfrum,<sup>2</sup> and the ASDEX Upgrade Team<sup>2</sup>

<sup>1</sup>Center for Energy Research, University of California of San Diego, 9500 Gilman Drive, M/C 0417, La Jolla, CA 92093, USA

<sup>2</sup>Max Planck Institute for Plasma Physics, Boltzmannstr. 2, 85748 Garching, Germany

<sup>3</sup>Physics Department E28, Technical University of Munich, 85747 Garching, Germany

<sup>4</sup>FOM-Institute DIFFER, Association EURATOM-FOM, NL-3439MN, Nieuwegein, The Netherlands

(Dated: 4 March 2014)

A reciprocating Langmuir probe was used to directly measure the behavior of turbulence and flows in the X-point region during transitions between low- ( $L$ ) and high-confinement ( $H$ ) mode in ASDEX Upgrade. The probe traverses the divertor horizontally in 140 ms, typically 2-5 cm below the X-point. Toroidal Mach number, density, floating potential ( $\phi_f$ ) and electron temperature ( $T_e$ ) are measured. In the regime accessible to the probe ( $P_{\text{inj}} < 1.5$  MW, line-integrated core density  $< 4 \times 10^{19}$  m<sup>-2</sup>), the  $L$ - $H$  transition features an intermediate phase ( $I$ -phase), characterized by limit-cycle oscillations (LCO) at 0.5-3 kHz [G.D. Conway *et al.*, PRL **106**, 065001 (2011)]. The probe measurements reveal that this pulsing affects both the density and the toroidal Mach number. It is present in both the low- (LFS) and high-field sides (HFS) of the scrape-off layer, while high-amplitude broadband turbulence usually dominates the private-flux region. Profile comparisons between  $L$ -mode and  $I$ -phase show lower density in pulsing regions and small shifts in  $T_e$ , directed oppositely on LFS and HFS, which are compensated by shifts in  $\phi_f$  to yield a surprisingly unchanged plasma potential profile. Directly observed  $L$ - $I$ -phase transitions reveal that the onset of the pulsing is preceded by a fast 50% density drop in the HFS X-point region. Back transitions to  $L$ -mode occur essentially symmetrically, with the pulsing stopping first, followed by a fast recovery to  $L$ -mode density levels in the divertor.

## I. INTRODUCTION

It is well established that the interaction between shear flows and turbulence is the dominant mechanism responsible for the  $L$ - $H$  transition in tokamaks.<sup>1-13</sup> While this interaction is primarily important in the confined plasma, several observations have been made that relate the  $L$ - $H$  transition to properties of the scrape-off layer (SOL),<sup>14,15</sup> neutrals, or even the wall.<sup>16</sup> It is thus possible that theories and models based on turbulence-flow interaction alone will be incomplete when it comes to predicting the  $L$ - $H$  power threshold in future devices such as ITER.

To investigate any such additional ingredients related to SOL and divertor physics that might be relevant for a predictive model of the  $L$ - $H$  transition, this paper reports on a series of experiments in ASDEX Upgrade, where a reciprocating Langmuir-Mach probe was employed to measure properties of profiles, flows, and turbulence, in the X-point region across  $L$ - $H$  transitions. A naturally emerging focus consisted of the intermediate phase between  $L$ -mode and  $H$ -mode, referred to as “ $I$ -phase”, which was almost universally observed in the studied experimental regimes that were compatible with probe operations.  $I$ -phases in AUG<sup>1,2,17,18</sup> and elsewhere<sup>3-5,8,10,11,19,20</sup> are characterized by a strong “pulsing” activity at frequencies of a few kHz, which has been attributed to the predator-prey interplay between shear flows and turbulence.<sup>1,3-5,8-13</sup>

The paper is organized as follows: Section II reviews the main diagnostics at ASDEX Upgrade used for this

work, namely the reciprocating X-point probe and the V-band Doppler reflectometry system. General properties of the experimental discharges are presented in Sec. III. Section IV focuses on profile comparisons between  $L$ -mode and  $I$ -phase. Direct probe observations of  $L$ - $I$ -phase transitions and  $I$ -phase- $L$  back transitions are discussed in Sec. V. Properties of the  $I$ -phase pulsing are investigated in Sec. VI. The main results are summarized in Sec. VII.

## II. DIAGNOSTICS

### A. The reciprocating X-point probe at ASDEX Upgrade

The reciprocating X-point probe is installed at  $z = -0.996$  m in Sector 10 of ASDEX Upgrade (Fig. 1).<sup>23-25</sup> It reciprocates horizontally through the divertor entrance, taking about 140 ms to cover the distance between the LFS wall at a major radius of  $R = 1.645$  m and the point of maximum insertion at  $R = 1.305$  m, thus stopping only 1.5 cm short of the HFS wall (Fig. 1). For typical equilibria, the probe trajectory falls below the X-point by about 2-5 cm, although data at the X-point was also obtained occasionally. The probe has a motor-drive system, for which up to six plunges per shot can be individually configured, in particular allowing for different stroke depths per plunge. In practice, heating of the probe tips limits the number of useful plunges to about three.

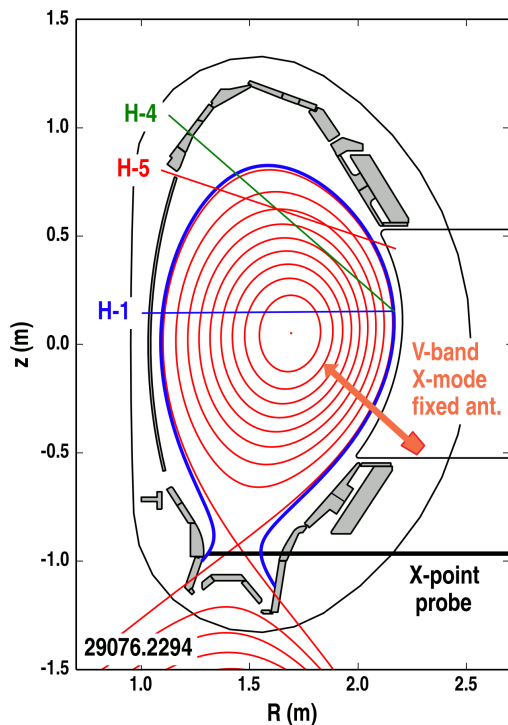


FIG. 1.  $X$ -point probe at maximum insertion in discharge 29076 at 2.294 s, during the first of three plunges. The field line connected to the probe tips is shown in blue (connection lengths: 65.39 m and 1.79 m to the LFS/HFS divertor, respectively). Also shown are the lower antenna of the  $V$ -band Doppler reflectometry system<sup>1,2,21</sup> and the interferometry chords H-1, H-4 and H-5.<sup>22</sup>



FIG. 2. Photograph of the probe head entering the vessel, viewed from the top. The diameter of the graphite probe shaft is 2 cm. The cylindrical graphite tips have a diameter of 0.9 mm and a length of approximately 3 mm. The two bottom tips are separated by a graphite barrier.

The probe head is equipped with three cylindrical graphite tips (Fig. 2), typically 0.9 mm in diameter and 2-3 mm in length. The upper, freestanding tip (closest to the camera view in Fig. 2) was usually swept at 1 kHz in the range of -200 V to +50 V (maximum current 1 A) to measure DC profiles of floating potential and electron temperature. The lower two tips are separated by a

barrier to form a Mach probe, which is aligned horizontally to measure the toroidal flow component.<sup>26-31</sup> For the experiments reported here, the Mach probe was DC biased to -200 V (maximum current 4 A) to measure turbulent fluctuations at a sampling rate of 0.5 MHz. When DC biasing the probe, arcing can usually not be avoided, in particular when entering the HFS SOL, which is usually characterized by a high density.<sup>32,33</sup> To limit long burning arcs, a protection system was installed which disconnects the power supply if a current threshold is exceeded, restoring the connection after a delay of either 2 or 10 ms. This protection system was used in some of the discharges presented here (e.g., Fig. 9).

## B. The $V$ -band Doppler reflectometry system

The  $V$ -band Doppler reflectometry system, described in detail in Refs. 2, 21, and 1, launches an  $X$ -mode polarized wave in the 50-75-GHz range from the lower launcher depicted in Fig. 1, at a small angle  $\theta_0$  with respect to the direction of the density gradient, which is reflected at the cutoff layer where  $N^2(n_e, f_0) = \sin^2 \theta_0$ . The injected frequency  $f_0$  can be stepped typically every 3-20 ms to change the radial location of the measurement, taking about 0.5 ms for the switching process, during which no measurements are available. If  $n_e$  fluctuations exist on the cutoff layer at a wavenumber  $k_\perp = 2k_0 \sin \theta_0$ , the Bragg-refracted signal of order  $m = -1$  is backscattered to the launch location, where it is collected by a receiver antenna adjacent to the launcher. The intensity of the backscattered signal is thus proportional to the turbulence intensity  $S(k_\perp) \propto \tilde{n}_e^2$ , at wavenumber  $k_\perp$ , at the location of the cutoff layer. In addition, if the fluctuations propagate at a velocity  $\mathbf{u}$ , the backscattered signal will be Doppler shifted by  $2\pi f_D = \mathbf{k} \cdot \mathbf{u} \approx \mathbf{k}_\perp \cdot \mathbf{u}_\perp$ . After heterodyne detection of the complex signal, a windowed Fourier transform is applied to obtain the time- and frequency-resolved intensity  $S(t, f_D)$ , where  $|f_D| \leq 2$  MHz. This is then analyzed further to extract the mean velocity  $u_\perp(t)$  and the instantaneous turbulence intensity  $S_{\text{turb}}(t)$ .

## III. DESCRIPTION OF THE EXPERIMENT

A series of experiments were performed at the ASDEX Upgrade tokamak to obtain  $X$ -point probe measurements in  $L$ -mode,  $H$ -mode and in  $I$ -phases. A typical discharge is shown in Fig. 3, where five  $L$ - $H$  and  $H$ - $L$  transitions were produced by modulating 800 kW of ECRH power at a period of 800 ms with 50% duty cycle. Beam blips were used in some discharges to obtain toroidal rotation and ion temperature data. A line-integrated core density around  $3 \times 10^{19} \text{ m}^{-3}$  was chosen as a compromise between lowest possible  $L$ - $H$  transition power threshold (minimum at about  $4 \times 10^{19} \text{ m}^{-3}$ )<sup>16,34,35</sup> and probe arcing, which was found to occur less or later at lower den-

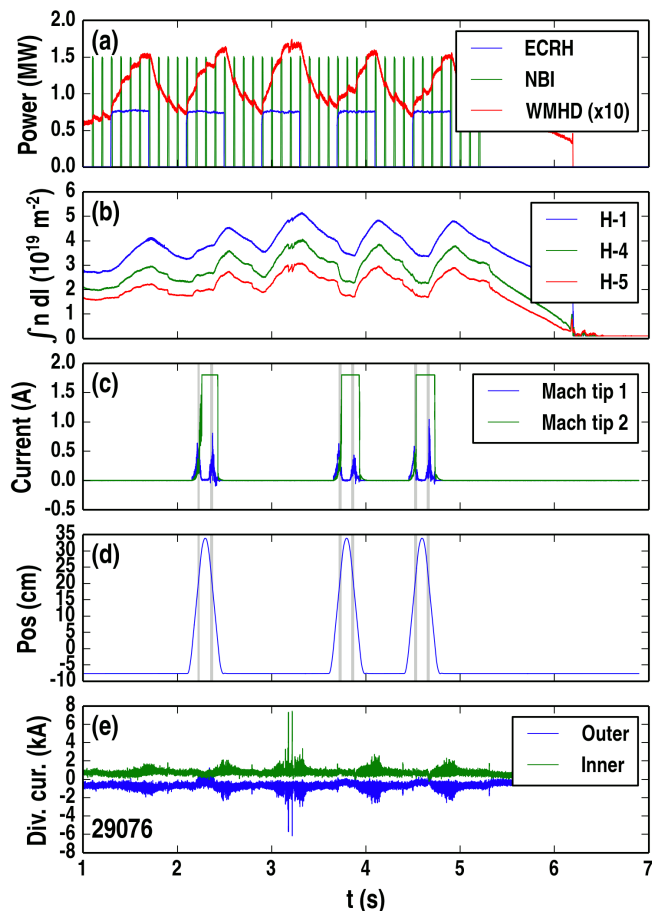


FIG. 3. Typical discharge behavior. (a) ECRH and NBI heating pulses and plasma stored energy. (b) Line-integrated density measured by three interferometer channels. (c) Mach probe currents. (d) Probe distance from the LFS wall. Shaded bars indicate the position of the private flux region. (e) Divertor shunt currents as an indicator of the  $L$ - $H$  transition.

sities. The plasma current was 800 kA and the toroidal magnetic field was usually -2.35 T, which was reduced to -1.8 T in some discharges to reduce the  $L$ - $H$  transition threshold even further.

The probe plunges were timed to catch up to three  $L$ - $H$  transitions at different locations in the SOL. Full plunges across the divertor entrance were attempted most of the time, which had about a 50% success rate to reach the dwell point at the HFS prior to arcing. When unsuccessful, arcing occurred mostly when going from the private-flux (PF) region into the HFS SOL, which usually features a steep climb in density. On the outward stroke, either arcing or tips entering a thermal electron-emission regime always occurred in these conditions. As opposed to similar measurements with the reciprocating midplane probe at DIII-D,<sup>30,31</sup> it was found that the  $X$ -point probe at ASDEX Upgrade can delay transitions from  $L$ -mode to  $I$ -phase, or induce back transitions from  $H$ -mode to an  $I$ -phase. However, no significant perturbations of the

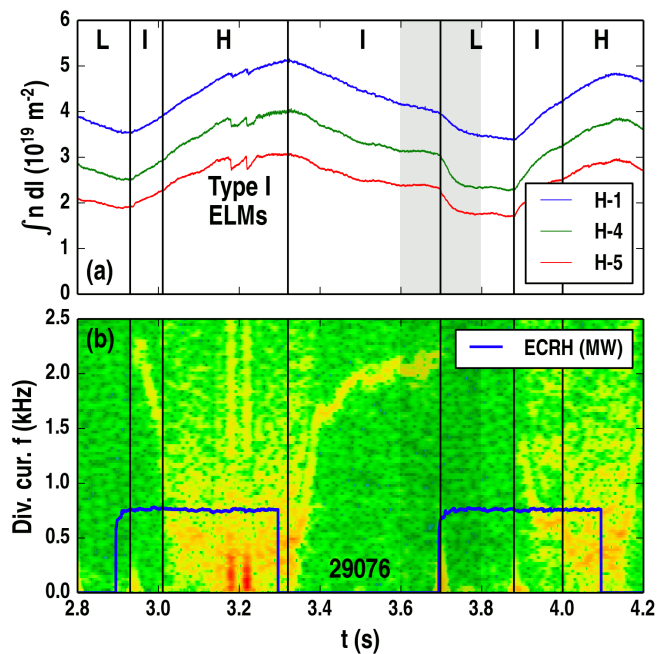


FIG. 4. Expanded view of an  $L$ - $H$ - $L$  transition cycle of Fig. 3, showing the  $I$ -phases. A smooth  $H$ - $I$ - $L$  back-transition sequence is observed. The shaded region is investigated in more detail in Fig. 6. (a) Line-integrated density. (b) Spectrogram of the inner divertor shunt current, together with the time trace of the ECRH power.

probe are usually seen if the plasma is far from a possible transition.

Figure 4 shows an expanded view of one  $L$ - $H$ - $L$  transition cycle of Fig. 3, together with a spectrogram of the inner divertor shunt current. Starting from a quiescent  $L$ -mode, it is evident that the  $L$ - $H$  transition proceeds via an  $I$ -phase, characterized by a pulsing activity starting at  $\sim 2.2$  kHz and chirping down to  $\sim 1.5$  kHz before the full  $H$ -mode is established, which is characterized by broadband spectral activity. The pulsing activity in the  $I$ -phase has been identified as predator-prey oscillations between shear flows and microturbulence.<sup>1,8</sup> The rise in the core plasma density typical for the  $H$ -mode already starts at the beginning of the  $I$ -phase, sometimes with a second change in slope at the full transition. In the low-density conditions studied here,  $I$ -phases were always seen in  $L$ - $H$  transitions.

The discharge in Fig. 4 is remarkable in that it also features a smooth back transition from  $H$ -mode to an  $I$ -phase, without an ELM-like event. After two type-I ELMs in the  $H$ -mode, the ECRH power is switched off at 3.3 s. Already 20 ms later, the  $H$ -mode transitions to an  $I$ -phase by undergoing essentially the reverse series of events: The pulsing reappears at  $\sim 0.5$  kHz, chirping up to  $\sim 2$  kHz as the core density decreases. At about 3.4 s, the  $I$ -phase is stabilized and supported only by beam blips for an additional 300 ms until the  $I$ - $L$  transition finally happens at 3.698 s. This illustrates the highly

stable nature of the  $I$ -phase, which has already been demonstrated to be sustainable over the whole discharge length.<sup>1</sup> The time of the  $I$ - $L$  back transition occurs 2 ms before the onset of the next ECRH pulse, which was also accompanied by a probe plunge (the probe data will be presented later in Fig. 6). The pulsing activity at  $\sim 2$  kHz stops and the core density decreases at a much higher rate than after the  $H$ - $I$  back transition, until a steady-state  $L$ -mode is achieved. At 3.88 s, the ECRH produces again an  $L$ - $I$  transition and the cycle repeats. This discharge illustrates that the sequence of events in an  $L$ - $I$ - $H$  transition is undergone in exact reverse order in a smooth  $H$ - $I$ - $L$  back transition.

#### IV. COMPARISON OF L-MODE AND I-PHASE PROFILES

In this Section, we present a comparison between the  $L$ -mode and  $I$ -phase profiles at the divertor entrance, obtained in back-to-back repeat shots with the reciprocating  $X$ -point probe. Shot 29311 had an  $L$ - $I$  transition when the probe was still close to the LFS wall, thus obtaining  $I$ -phase data during most of the plunge. The discharge was repeated identically in shot 29312, only the probe plunge was set 50 ms earlier. The  $L$ - $I$  transition happened only when the probe was already far on the HFS. The combination of these two shots is thus very well suited for profile comparisons between  $L$ -mode and  $I$ -phase.

The results are shown in Fig. 5 in terms of ion saturation current ( $I_{\text{sat}}$ ), toroidal Mach number, floating potential ( $\phi_f$ ), electron temperature ( $T_e$ ), plasma potential ( $\phi = \phi_f + 2.8T_e$ ) and electric field along the major radius ( $E_R = -\partial\phi/\partial R$ ), as a function of major radius  $R$ . Here, the  $I_{\text{sat}}$  measurement is the sum of the DC coupled Mach tips, which agrees reasonably well with the  $I_{\text{sat}}$  part of the swept single tip. The Mach number is evaluated instantaneously as<sup>26,31</sup>

$$M = \frac{1}{2} \log \frac{I_-}{I_+}, \quad (1)$$

where  $I_{\pm}$  are the currents drawn by the two equally-sized Mach tips. Positive Mach numbers are in the  $+\varphi$  direction in a cylindrical coordinate system. Given that the plasma current is in the  $+\varphi$  and the toroidal magnetic field in the  $-\varphi$  direction in ASDEX Upgrade, flows towards the divertor have negative sign on the LFS and positive sign on the HFS. The  $I_{\text{sat}}$  and Mach number measurements are available at 250 kHz bandwidth with very good signal to noise ratio. In contrast, the  $\phi_f$  and  $T_e$  measurements are available at twice the sweep frequency of 1 kHz ( $L$ -mode case) and 0.7 kHz ( $I$ -phase case) at most. Since this is comparable to the pulsing frequency in  $I$ -phases (the sweep frequency was varied to exclude a possible locking of the  $I$ -phase pulsing to the probe bias), Langmuir characteristic fits are especially challenging.

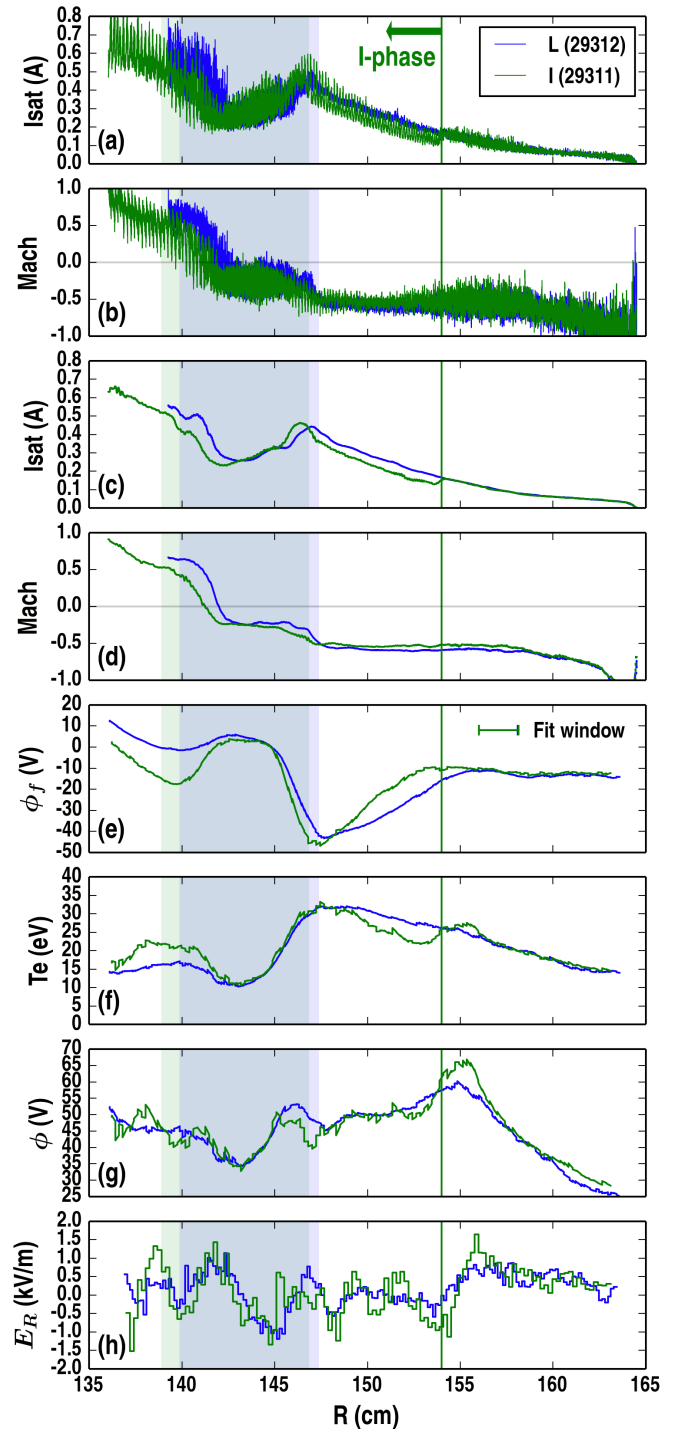


FIG. 5. Profile comparison between  $L$ -mode and  $I$ -phase in back-to-back repeat shots. The PF region is obtained accurately from CLISTE EQI equilibria and shown as shaded areas. (a, b) Ion saturation current and toroidal Mach number at full bandwidth. (c, d) Low-pass filtered ion saturation current and toroidal Mach number. (e) Floating potential  $\phi_f$ . (f) Electron temperature  $T_e$ . (g) Plasma potential  $\phi = \phi_f + 2.8T_e$ . (h)  $E_R = -\partial\phi/\partial R$ .

Using a special technique which allows the fit parameters to vary linearly, the fitted interval can be extended to many sweep periods without losing track of the background profile changes as the probe moves. In addition, using *orthogonal distance regression (ODR)*<sup>36</sup> instead of conventional least-squares optimization improves the result considerably in the presence of large-scale fluctuations. The details of this technique will be published separately. Here, it was applied to 7-ms-long overlapping windows, corresponding to  $\sim 2$  cm of probe motion and 14 (10) half-sweep periods for the  $L$ -mode ( $I$ -phase) case. The slopes determined by the fits are directly used for the calculation of  $E_R$ . The relatively long window was chosen as the best compromise between satisfactory averaging over the  $I$ -phase pulsing activity and sufficient smoothing for the  $E_R$  calculation, while keeping the smoothing of steep gradients at an acceptable level. The results discussed in the following are robust for a wide variety of time windows.

When the probe enters from the LFS, both plasmas are still in  $L$ -mode. All profiles agree very well up to  $R \simeq 156$  cm, illustrating the excellent reproducibility of the discharge. The high fluctuations in the Mach number are partially due to low signal at the downstream tip. There are also wall-proximity effects which lead to a too high Mach number close to the wall. These effects usually become unimportant once the connection length reaches 2-5 m, at which point a Mach number of -0.5 is typically observed on the LFS. The floating potential remains slightly negative and flat while  $T_e$  increases linearly with increasing distance to the wall.

At  $R = 155$  cm, a small but noticeable increase of  $T_e$  by merely  $\sim 3$  eV is observed in shot 29311. Due to the high multiplicative factor of 2.8, this has a significant effect on the inferred plasma potential in Fig. 5 (g), which in turn changes  $E_R$  and its shear in Fig. 5 (h). While still difficult to resolve from the experimental measurements, such a difference in the electric field shear could well be a factor for the following bifurcation of the two discharges.

At  $R = 154$  cm, the  $L$ - $I$  transition occurs in shot 29311, while discharge 29312 continues in  $L$ -mode. An immediate drop in  $I_{\text{sat}}$  occurs, closely followed by the onset of the pulsing, which appears to oscillate between the two density levels [Fig. 5 (a)]. The Mach number profiles are still very similar between  $L$ -mode and  $I$ -phase, with the pulsing weakly affecting the LFS Mach number. A significant change is observed in the floating potential, which becomes less negative in the  $I$ -phase compared to  $L$ -mode by about 10-15 V. The shift in the floating potential is accompanied by a reduced electron temperature by about 5 eV. The differences in the  $\phi_f$  and  $T_e$  profiles remarkably compensate to yield an approximately unchanged plasma potential profile.

Upon entering the PF region, all profiles are again similar, with  $T_e$  dropping to the 10 eV range and the Mach number changing sign as is usually observed. The pulsing in the  $I$ -phase is still visible but overlaid by high-amplitude broadband turbulence. Upon entering the

HFS SOL, the pulsing becomes very pronounced and is now also clearly visible in the Mach number. The mean density in the  $I$ -phase is lower than in  $L$ -mode, accompanied by a shift in  $\phi_f$  and  $T_e$  in the opposite direction than on the LFS. Again, these shifts compensate to yield approximately the same plasma potential.

Finally, it is important to observe that the plasma equilibrium evolves as the  $I$ -phase progresses, accumulating an inward shift of the  $X$ -point of about 5 mm by the time the probe has reached the inner divertor leg. This shift can partially account for the mismatch in the  $I_{\text{sat}}$  and Mach number profiles on the HFS. The change in equilibrium is associated with the slow evolution after the  $L$ - $I$  transition, not with a fast event at the transition, since we did not find any indications of such an event in the highest time-resolution equilibrium reconstruction available (CLISTE EQH equilibrium, with 1 ms time resolution).

In summary, the  $I$ -phase is characterized by a lower mean density in the SOL compared to  $L$ -mode, while the mean toroidal Mach number profiles do not change appreciably. In the  $I$ -phase, the plasma becomes cooler on the LFS and hotter on the HFS by about 5 eV. These shifts in  $T_e$  are remarkably balanced by shifts in  $\phi_f$ , such that the inferred plasma potential remains approximately unchanged, indicating that there are no significant differences in the average electric field between  $L$ -mode and  $I$ -phase in the  $X$ -point region. The density drop at the beginning of the  $I$ -phase occurs rapidly and appears to precede the onset of the pulsing, which will be investigated more closely in the following Section in terms of directly observed transitions.

## V. DIRECT OBSERVATIONS OF TRANSITIONS

Over the course of the 2012/2013 campaign, a significant number of transitions were directly observed with the  $X$ -point probe at various radial positions. Here, we present representative examples of  $L$ - $I$  and  $I$ - $L$  transitions from the LFS (Fig. 6) and the HFS (Fig. 7), where the latter example was taken from a compact  $L$ - $I$ - $L$  transition sequence within 65 ms. Two additional discharges are presented in Fig. 9 to demonstrate the reproducibility of the events.

Figure 6 shows expanded views of the  $L$ - $I$  transition from Fig. 5 and the  $I$ - $L$  back transition from Fig. 4, both occurring when the probe was on the LFS. As described earlier in Sec. IV, the  $L$ - $I$  transition features a SOL density drop concurrent with the begin of the density rise in the core [Fig. 6 (a, c)]. The pulsing becomes clearly visible only after the density drop, although there may be some low-frequency fluctuation activity present prior to the drop, which could already indicate zonal flow activity. Unfortunately, no usable Doppler reflectometry data is available for a shot where the  $X$ -point probe observed the  $L$ - $I$  transition on the LFS, such that no comparison of the two diagnostics could be carried out for this case.

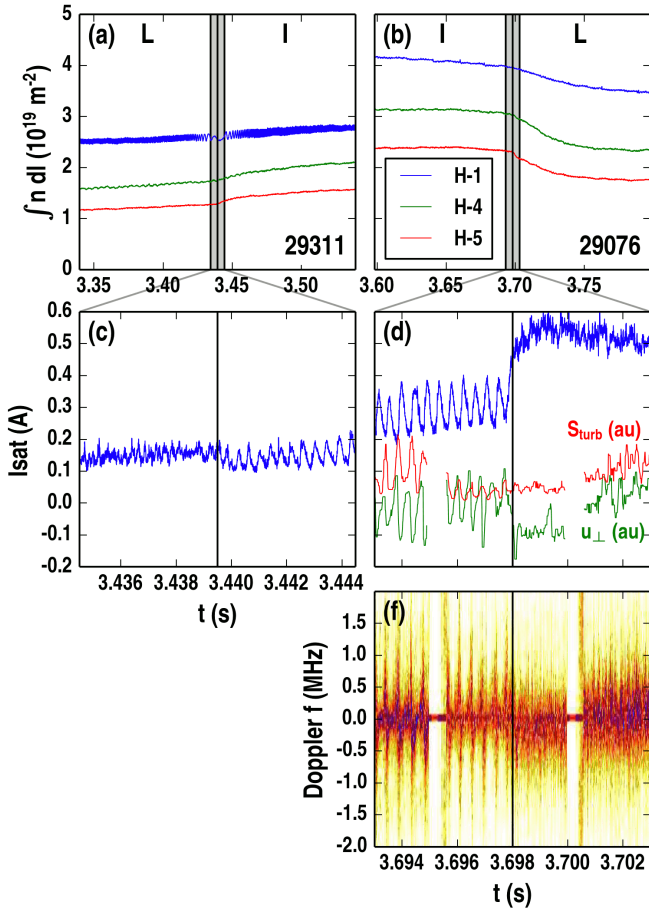


FIG. 6.  $L$ - $I$  (a, c) and  $I$ - $L$  transitions (b, d, f) on the LFS. (a, b) Line-integrated core density. (c, d) Total ion saturation current measured by the Mach probe, in (d) together with  $u_{\perp}$  and  $S_{\text{turb}}$  measured by Doppler reflectometry at the outboard midplane, using three consecutive frequencies corresponding to cutoff locations at  $\rho_{\text{pol}} \simeq 0.995$ ,  $0.993$  and  $0.990$  ( $\pm 0.005$  or  $\pm 2$  mm), close to the  $E_r$ -well minimum. The missing regions are due to frequency switching. (f) Windowed FFT of the raw Doppler reflectometry signal.

In Fig. 6 (a), it is interesting to note that a core MHD mode, visible in the innermost interferometer chord H-1, slows down substantially before the  $L$ - $I$  transition and accelerates again after the transition. There are at least two other discharges with core MHD modes showing this behavior, indicating that it may hold information on changes in the core plasma in the vicinity of the  $L$ - $I$  transition. It appears worthwhile to investigate this phenomenon more closely in the future.

In Fig. 6 (b, d, f), data from the  $X$ -point probe and the Doppler reflectometry system is presented for the smooth  $I$ - $L$  back transition from Fig. 4. Both diagnostics see a sudden stop of the pulsing, followed by a strong density rise for the probe, surpassing the amplitude of the  $I$ -phase pulsing by a factor of two, and a strong shift in  $u_{\perp}$  for the Doppler reflectometry system. No indications that the pulsing continues after the transition exist in either

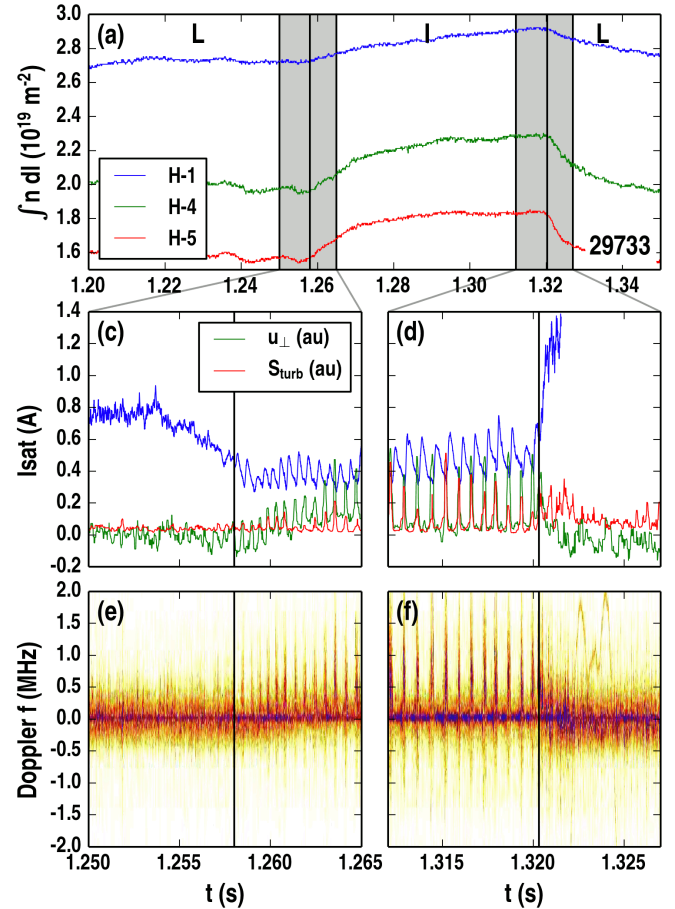


FIG. 7. As in Fig. 6 for an  $L$ - $I$ - $L$  transition sequence on the HFS. The density to the HFS of the  $X$ -point starts dropping 4 ms before the first indications of the  $I$ -phase pulsing appear both in the Doppler reflectometry (cutoff layer at  $\rho_{\text{pol}} \simeq 0.960$ ) and the  $X$ -point probe data.

diagnostic. The density rise in the SOL appears to occur concurrently with the first indications of a dropping core density in the interferometer signals. During the  $I$ -phase pulsing, the  $I_{\text{sat}}$  measurements of the probe are out of phase with both the  $u_{\perp}$  and  $S_{\text{turb}}$  measurements of the Doppler reflectometry system, which will become even clearer for the HFS SOL measurements presented in the following.

Figure 7 shows a compact  $L$ - $I$ - $L$  transition sequence, which the probe observed between  $R = 135$  cm and  $R = 131$  cm, on the approach to the HFS turning point. Excellent data are available from both the probe and the Doppler reflectometry system. At the  $L$ - $I$  transition in Fig. 7 (c), the density drop starts approximately 4 ms before the first indication of the pulsing appears. The pulsing behavior is consistent with the observations on the LFS, namely a chirping behavior from higher to lower frequencies and increasingly triangular waveforms. After approximately 65 ms of  $I$ -phase, during which the average density has slightly increased, the back transition to  $L$ -mode occurs with a massive return of  $L$ -mode

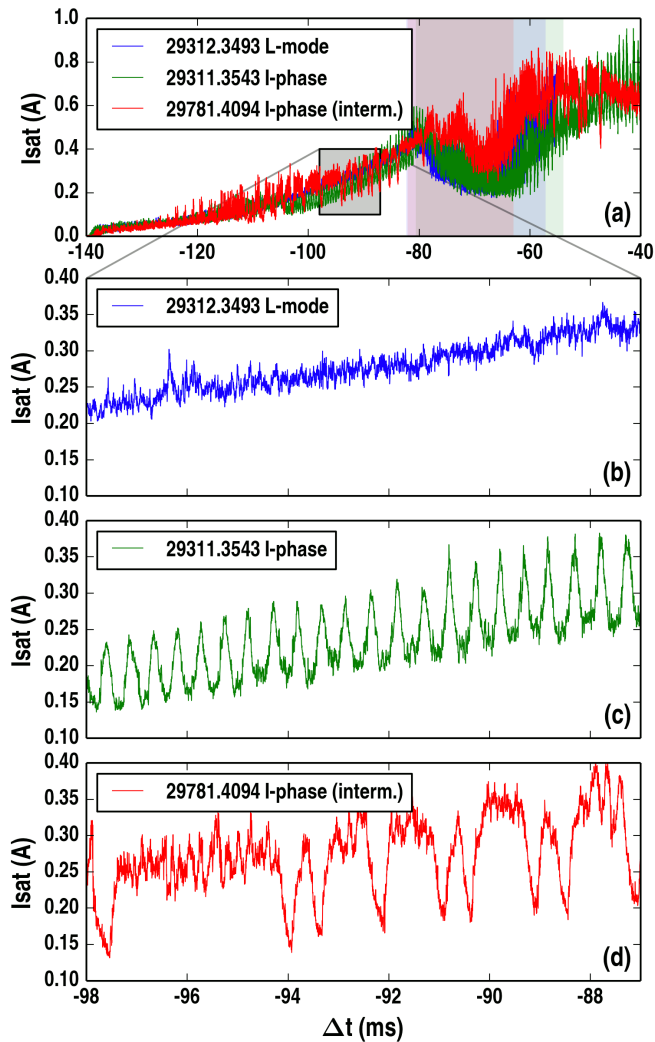


FIG. 8. (a) Comparison of ion saturation current time traces for the  $L$ -mode and  $I$ -phase cases in Fig. 5, together with an example of an intermittent  $I$ -phase. (b, c, d) Expanded views of (b) the  $L$ -mode, (c) the  $I$ -phase with fairly coherent pulses, and (d) the  $I$ -phase with intermittent pulses.

density levels [Fig. 7 (d)]. The dominant impression is again that the pulsing activity has essentially stopped before the density returns. The density return to the HFS SOL coincides with the strong drop in the line-integrated core density. The pulsing is very well correlated between the Doppler reflectometry data and the probe data, with regions of high  $|u_{\perp}|$  measured by Doppler reflectometry at the outboard midplane corresponding to phases of low ion saturation current measured by the probe in the HFS  $X$ -point region. The present analysis suggests that the time delays between the two diagnostics are smaller than the parallel transit time  $L_{\parallel}/c_s \approx 0.1$  ms between the outboard midplane and the  $X$ -point region, suggesting that the fluctuations in the divertor may play an integral role in the global dynamics of the  $I$ -phase pulsing.

## VI. PROPERTIES OF THE $I$ -PHASE PULSING

To investigate the nature of the pulsing more closely, Fig. 8 shows an expanded view of the  $I_{\text{sat}}$  traces in Fig. 5, together with an additional discharge, in which the  $I$ -phase pulsing occurred intermittently. Despite the usually highly coherent appearance of the  $I$ -phase pulsing, it is evident that single pulses can appear or be skipped without any prior indications of mode growth or damping. Linear mode physics, in which some equations are linearized and Fourier transformed to obtain a dispersion relation, is unable to describe such a behavior. This highlights the nonlinear nature of the  $I$ -phase pulsing and is consistent with the interpretation as predator-prey oscillations.<sup>1,8</sup>

It is interesting to note that the pulse shapes in Fig. 8 (c) appear to be pointed upward, while those in (d) appear to be pointed downward. Equivalently, more time is spent in the lower-density state in (c) and in the higher-density state in (d). Indeed, both varieties of limit-cycle oscillations were found also in other discharges. One may speculate that the direction of pointedness of the LCOs may contain information on the relative stability of the two limit states.

A topic of considerable interest is whether there is any relation between the  $I$ -phase pulsing and the small-scale turbulence remaining in the SOL. Since the main region of importance of zonal flows lies in the core plasma, this is not necessarily expected. However, indications of a modulation of the high-frequency turbulence with the low-frequency pulsing have been found in the raw probe data, which warrants a deeper investigation.

To separate the high-frequency turbulence from the low-frequency waveforms of the pulsing we proceed as follows. The first (and tricky) step is to choose a cutoff frequency, which must be sufficiently high so that the non-sinusoidal waveform of the pulsing is well described by the low-pass filtered signal. Although the fundamental pulsing frequency is only 1-2 kHz, inclusion of Fourier components up to 10 kHz appears necessary to properly follow the triangular waveforms. Hence, a cutoff frequency of 10 kHz was chosen, and the  $I_{\text{sat}}(t)$  signal was filtered with both low-pass and high-pass zero-phase filters, yielding two new signals denoted as  $I_{\text{sat}}^{<10\text{kHz}}(t)$  and  $I_{\text{sat}}^{>10\text{kHz}}(t)$ . The high-pass filtered signal was squared and boxcar-averaged over a timescale of 40  $\mu\text{s}$ , and the square-root was taken to obtain  $I_{\text{sat}}^{>10\text{kHz}, \text{rms}}(t)$ , which is a measure of the instantaneous strength of fluctuations above 10 kHz. Both signals were detrended and the windowed cross correlation was calculated using a window length of 4096 points, corresponding to about 8 ms.

This analysis was applied in Fig. 9 to an  $L$ - $I$ - $L$  transition with the  $X$ -point probe on the LFS (a, c, e) and an  $L$ - $I$  transition with the probe on the HFS (b, d, f). The raw  $I_{\text{sat}}$  signals are shown in (a, b), as a function of both the time coordinate  $t$  and the probe major radius coordinate  $R(t)$ . The spectrograms in (c, d) show the frequency evolution of the  $I$ -phases, which, after an

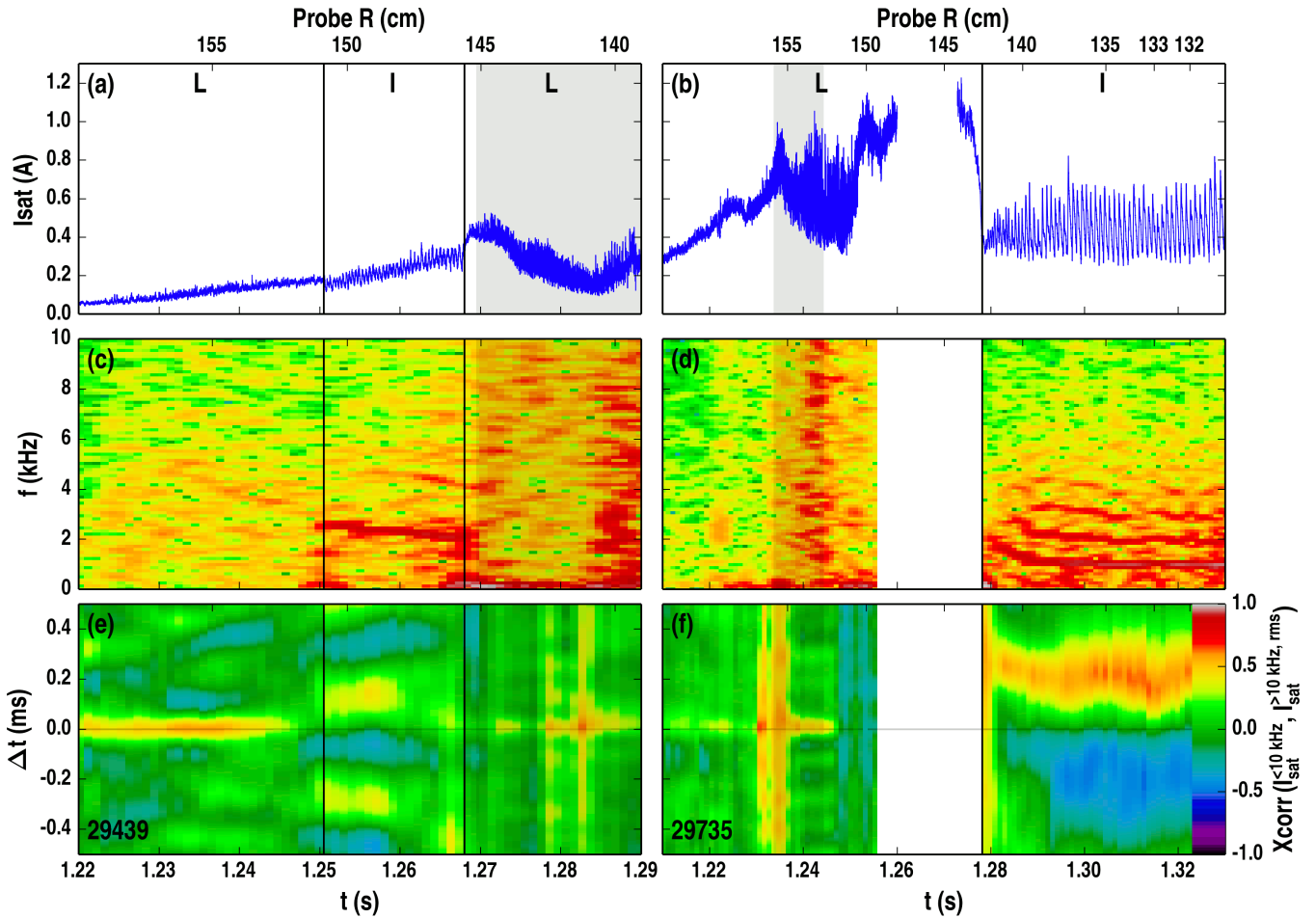


FIG. 9. Additional data sets for an  $L$ - $I$ - $L$  transition sequence on the LFS (a, c, e) and an  $L$ - $I$  transition on the HFS (b, d, f). Shaded regions correspond to the PF region. The missing data on the HFS is due to action of the arc mitigation system, which recovered the measurements at 1.275 s. A particularly strong density drop on the HFS is visible prior to the onset of the  $I$ -phase pulsing. (a, b) Total ion saturation current. (c, d) Spectrograms. (e, f) Windowed cross correlation between the low-pass filtered ( $< 10$  kHz)  $I_{\text{sat}}$  signal and high-pass filtered ( $> 10$  kHz) rms fluctuation level in the same signal. In  $I$ -phases, correlations reach 0.6 and cross phases are between  $\pi/2$  and  $\pi$ , with the low-pass filtered signal lagging behind the small-scale turbulence.

initial downward chirping phase, reach fundamental frequencies of  $\sim 2$  kHz and  $\sim 1$  kHz for the LFS/HFS cases, respectively. Higher harmonics appear later, one in the LFS case (c) and up to three for the HFS case (d), a manifestation of the evolution from sinusoidal to triangular waveforms. The spectrograms support the choice of the cutoff frequency of 10 kHz. The results for the windowed cross correlation function are shown in Fig. 9 (e, f). It is evident that the cross correlation function follows a periodic pattern in the  $I$ -phases, establishing the important result that the small-scale turbulence is modulated during the limit-cycle oscillations also in the SOL. The time delays at maximum correlation, which can reach 0.6, correspond to a phase shift between  $\pi/2$  and  $\pi$ , with the low-frequency  $I_{\text{sat}}$  signal lagging behind the high-frequency turbulence.

A popular way to represent the phase relationship between a measure of the turbulence strength and a slowly-

varying system property is a Lissajous curve.<sup>10,11</sup> In our case, a straightforward plot of  $I_{\text{sat}}^{>10 \text{ kHz, rms}}$  against  $I_{\text{sat}}^{<10 \text{ kHz}}$  over many pulsing periods results in an unimpressive figure, due to the relatively low correlation of 0.6. To make progress, the average waveform of both signals during one oscillation period must be established before the Lissajous curve can be defined meaningfully in terms of these period-averaged signals.

In Fig. 10 (a), a 15-ms long sequence has been selected from the relatively stationary  $I$ -phase in Fig. 9 (b) and the signals  $I_{\text{sat}}^{<10 \text{ kHz}}$  and  $I_{\text{sat}}^{>10 \text{ kHz, rms}}$  have been formed. The best definition for the begin of each period appears to be the time at which the steep flank crosses the average signal level. Since the period length is not constant, each period is stretched to match the average period length before the point-wise average and standard deviation of the 15 period-realizations are calculated for the two signals. Three periods of the average waveforms are shown

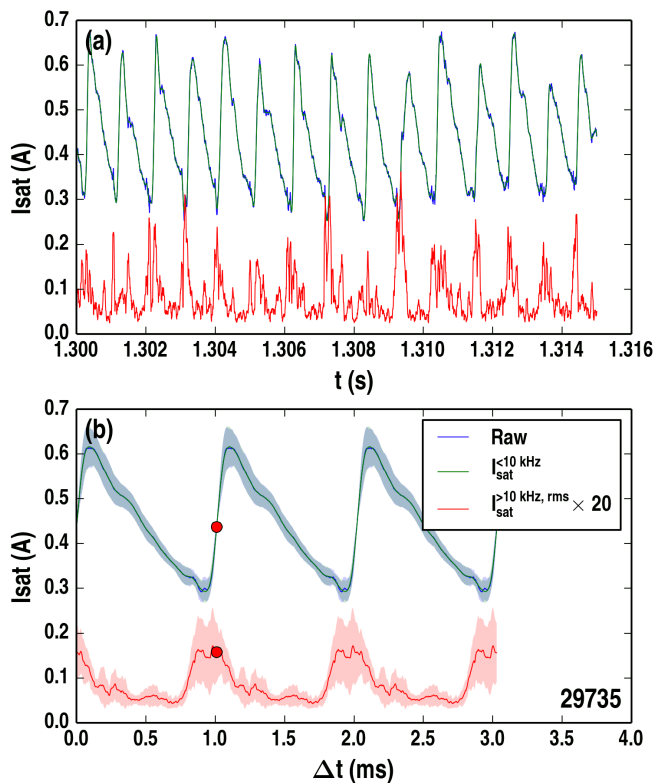


FIG. 10. (a) Expanded view of the fully developed  $I$ -phase from Fig. 9 (b). (b) Three periods of the average waveforms. Error estimates are calculated from the standard deviation of the averaging process. The starting point is marked by a red dot.

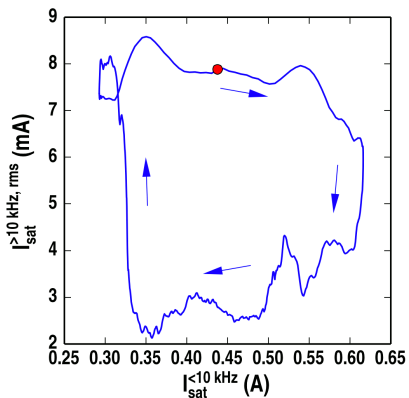


FIG. 11. Lissajous curve for the average waveforms in Fig. 10 (b). The starting point is again marked by a red dot.

in Fig. 10 (b), using the standard deviation as an error estimate. The average phase relationship between  $I_{\text{sat}}^{<10 \text{ kHz}}$  and  $I_{\text{sat}}^{>10 \text{ kHz, rms}}$  can now be meaningfully visualized as a Lissajous curve, which is given in Fig. 11. The Lissajous curve describes approximately a circle rotating in the clockwise direction, meaning that  $I_{\text{sat}}^{<10 \text{ kHz}}$  is following  $I_{\text{sat}}^{>10 \text{ kHz, rms}}$ . To discuss this result in the light of existing predator-prey models of shear-flow tur-

bulence interaction,<sup>6,10,11,13</sup> recall that we found a high degree of anti-correlation between  $I_{\text{sat}}$  and  $|u_{\perp}| \propto |E_r|$  at the outboard midplane in Fig. 7 (d). Thus the Lissajous curve between  $|E_r|$  and  $I_{\text{sat}}^{>10 \text{ kHz, rms}}$ , as presented in Ref. 11, would be followed in the counter-clockwise direction, corresponding to *type J* LCOs in their terminology. We have not observed a change in the LCO temporal ordering in the proximity of the  $L$ - $H$  transition. In fact, throughout our database, we have not yet found a case where the Lissajous curve is followed in the opposite direction (*type Y* LCOs). However, it is clear that the  $I_{\text{sat}}$  signal was measured at a very different location than  $|E_r|$  in our case, such that a more global version of the predator-prey theory of the  $L$ - $H$  transition, which is presently in development,<sup>13</sup> would be necessary to properly compare to.

Finally, it is worth pointing out that the ratio  $I_{\text{sat}}^{>10 \text{ kHz, rms}}/I_{\text{sat}}^{<10 \text{ kHz}}$  was measured to be only  $\sim 1\%$  in a fully developed  $I$ -phase, which could only be resolved due to the exceptionally good S/N ratio of Langmuir probes compared to other turbulence diagnostics. As a further complication, the waveform in Fig. 10 (a) appears to have secondary features, namely a bump on the downward flank and a secondary trough before the start of the upward flank. These secondary features show up in the average waveform in Fig. 10 (b), meaning that they are period-to-period reproducible, while they do not appear to be shot-to-shot reproducible for different  $I$ -phases. It is questionable whether such features should be counted as part of the average waveform or as part of the turbulence, which boils down to the choice of the cutoff frequency. While the shape of the Lissajous curve in Fig. 11 obviously depends on such choices, the result of a clockwise rotation direction appears to be robust for all  $I$ -phases, since we have not found a case with counter-clockwise rotation in our database.

## VII. DISCUSSION AND CONCLUSIONS

A comprehensive data set of  $L$ - $I$  transitions and  $I$ - $L$  back transitions was obtained with the reciprocating  $X$ -point probe in ASDEX Upgrade. The pulsing activity that defines the  $I$ -phase is strongly visible in the ion saturation currents measured by the probe and correlates strongly with Doppler reflectometry measurements at the outboard midplane, as well as with the divertor-tile shunt currents, highlighting the global nature of this phenomenon. Mean profile comparisons between  $L$ -mode and  $I$ -phase show small differences in parallel SOL flows and in the plasma potential  $\phi$ , although the mix between  $\phi_f$  and  $T_e$  contributions to  $\phi$  changes appreciably. Electrons are cooler on the LFS and hotter on the HFS in the  $I$ -phase by  $\sim 5$  eV. The strongest change is observed in terms of a significantly lower SOL density in the  $I$ -phase, particularly on the HFS. This is in fact consistent with the majority of reports on the  $I$ -phase, where a clear drop in the  $D_{\alpha}$  intensity is seen<sup>1,8,9,17-20</sup> prior to the main

pulsing activity, for which strong evidence exists that it results from the predator-prey interplay between shear flows and small-scale turbulence.

By observing in Fig. 8 (d) a case in which the pulsing occurred strongly intermittently, following an *all-or-nothing* principle, we add additional evidence that the pulsing cannot result from linear mode physics, thus corroborating the interpretation as an intrinsically nonlinear phenomenon. This paper also confirms that the *I*-phase pulsing does have a modulation effect on the smaller-scale fluctuations, even in the SOL, finding that the slowly-varying  $I_{\text{sat}}$  signal lags behind the small-scale turbulence by a phase shift between  $\pi/2$  and  $\pi$ . Although the phase relationship between the  $I_{\text{sat}}$  signal in the HFS *X*-point region and  $|E_r|$  measurements at the outboard midplane could be determined in Fig. 7 (d) as close to  $\pi$ , it is not evident to draw stronger conclusions due to the spatial separation of our measurements. Rather, our multi-point measurements combining two turbulence diagnostics may serve as a guidance for theorists towards the development of a global model of the *I*-phase and the *L-H* transition.

Perhaps the biggest challenge to the predator-prey model of the *L-H* transition from our data comes from the observation that a strong density drop in the SOL, especially on the HFS, precedes the onset of the first clearly identifiable pulse of the *I*-phase. If indeed a substantial change in the SOL density occurs before a change in the turbulence characteristics is observed, it would appear necessary to invoke an additional mechanism, other than the standard shear-flow turbulence interaction, to fully explain the observations. However, although it is clear that no change in the turbulence is observed in the Doppler reflectometry data before the SOL density drop in Fig. 7 (c), small indications appear to exist in the probe data, which have a superior S/N ratio. For example, in the spectrogram in Fig. 9 (c), there appears to be a weak indication that the spectral feature that will become the *I*-phase pulsing is already emerging prior to the density drop, such that a change of the turbulent transport could be invoked to reconcile the observations. To gain clarity on this important question, a more detailed investigation on the evolution of fluctuations prior to the SOL density drop will be carried out in the future.

<sup>1</sup>G. D. Conway, C. Angioni, F. Ryter, P. Sauter, J. Vicente, and the ASDEX Upgrade Team, *Phys. Rev. Lett.* **106**, 065001 (2011).

<sup>2</sup>G. D. Conway, E. Poli, T. Happel, and the ASDEX Upgrade Team, *Plasma and Fusion Research* **5**, S2005 (2010).

<sup>3</sup>T. Estrada, T. Happel, C. Hidalgo, E. Ascasíbar, and E. Blanco, *Europhys. Lett.* **92**, 35001 (2010).

<sup>4</sup>T. Estrada, C. Hidalgo, T. Happel, and P. H. Diamond, *Phys. Rev. Lett.* **107**, 245004 (2011).

<sup>5</sup>G. S. Xu, B. N. Wan, H. Q. Wang, H. Y. Guo, H. L. Zhao, A. D. Liu, V. Naulin, P. H. Diamond, G. R. Tynan, M. Xu, R. Chen, M. Jiang, P. Liu, N. Yan, W. Zhang, L. Wang, S. C. Liu, and S. Y. Ding, *Phys. Rev. Lett.* **107**, 125001 (2011).

<sup>6</sup>P. Manz, M. Ramisch, and U. Stroth, *Phys. Rev. E* **82**, 056403 (2010).

<sup>7</sup>U. Stroth, P. Manz, and M. Ramisch, *Plasma Phys. Control. Fusion* **53**, 024006 (2011).

<sup>8</sup>L. Schmitz, L. Zeng, T. L. Rhodes, J. C. Hillesheim, E. J. Doyle,

R. J. Groebner, W. A. Peebles, K. H. Burrell, and G. Wang, *Phys. Rev. Lett.* **108**, 155002 (2012).

<sup>9</sup>M. Xu, G. R. Tynan, P. H. Diamond, P. Manz, C. Holland, N. Fedorczak, S. C. Thakur, J. H. Yu, K. J. Zhao, J. Q. Dong, J. Cheng, W. Y. Hong, L. W. Yan, Q. W. Yang, X. M. Song, Y. Huang, L. Z. Cai, W. L. Zhong, Z. B. Shi, X. T. Ding, X. R. Duan, Y. Liu, and HL-2A team, *Phys. Rev. Lett.* **108**, 245001 (2012).

<sup>10</sup>P. Manz, G. S. Xu, B. N. Wan, H. Q. Wang, H. Y. Guo, I. Cziegler, N. Fedorczak, C. Holland, S. H. Müller, S. C. Thakur, M. Xu, K. Miki, P. H. Diamond, and G. R. Tynan, *Phys. Plasmas* **19**, 072311 (2012).

<sup>11</sup>J. Cheng, J. Q. Dong, K. Itoh, L. W. Yan, M. Xu, K. J. Zhao, W. Y. Hong, Z. H. Huang, X. Q. Ji, W. L. Zhong, D. L. Yu, S.-I. Itoh, L. Nie, D. F. Kong, T. Lan, A. D. Liu, X. L. Zou, Q. W. Yang, X. T. Ding, X. R. Duan, Y. Liu, and HL-2A team, *Phys. Rev. Lett.* **110**, 265002 (2013).

<sup>12</sup>K. Miki, P. H. Diamond, S.-H. Hahn, W. W. Xiao, O. D. Gürcan, and G. R. Tynan, *Phys. Rev. Lett.* **110**, 195002 (2013).

<sup>13</sup>G. R. Tynan, M. Xu, P. H. Diamond, J. Boedo, I. Cziegler, N. Fedorczak, P. Manz, K. Miki, S. Thakur, L. Schmitz, L. Zeng, E. J. Doyle, G. M. McKee, Z. Yan, G. S. Xu, B. N. Wan, H. Q. Wang, H. Guo, J. Dong, K. Zhao, J. Cheng, W. Hong, and L. W. Yan, *Nucl. Fusion* **53**, 073053 (2013).

<sup>14</sup>B. LaBombard, J. E. Rice, A. E. Hubbard, J. W. Hughes, M. Greenwald, J. Irby, Y. Lin, B. Lipschultz, E. S. Marmor, C. S. Pitchera, N. Smick, S. M. Wolfe, S. J. Wukitch, and the Alcator Group, *Nucl. Fusion* **52**, 1047 (2004).

<sup>15</sup>B. LaBombard, J. W. Hughes, N. Smick, A. Graf, K. Marr, R. McDermott, M. Reinke, M. Greenwald, B. Lipschultz, J. L. Terry, D. G. Whyte, S. J. Zweben, and the Alcator C-Mod Team, *Phys. Plasmas* **15**, 056106 (2008).

<sup>16</sup>F. Ryter, S. K. Rathgeber, L. Barrera Orte, M. Bernert, G. D. Conway, R. Fischer, T. Happel, B. Kurzan, R. M. McDermott, A. Scarabosio, W. Suttrop, E. Viezzer, M. Willensdorfer, E. Wolftrum, and the ASDEX Upgrade Team, *Nucl. Fusion* **53**, 113003 (2013).

<sup>17</sup>H. Zohm and the ASDEX Upgrade Team, *Phys. Rev. Lett.* **72**, 222 (1994).

<sup>18</sup>H. Zohm, F. Ryter, C. Fuchs, A. Herrmann, M. Kaufmann, J. Neuhauser, N. Salmon, and the ASDEX Upgrade Team, *Plasma Phys. Control. Fusion* **36**, A129 (1994).

<sup>19</sup>R. J. Colchin, M. J. Schaffer, B. A. Carreras, G. R. McKee, R. Maingi, T. N. Carlstrom, D. L. Rudakov, C. M. Greenfield, T. L. Rhodes, E. J. Doyle, N. H. Brooks, and M. E. Austin, *Phys. Rev. Lett.* **88**, 255002 (2002).

<sup>20</sup>R. J. Colchin, B. A. Carreras, R. Maingi, L. Baylor, T. C. Jernigan, M. J. Schaffer, T. N. Carlstrom, N. H. Brooks, C. M. Greenfield, P. Gohil, G. McKee, D. L. Rudakov, T. L. Rhodes, E. J. Doyle, M. E. Austin, and J. G. Watkins, *Nucl. Fusion* **42**, 1134 (2002).

<sup>21</sup>G. D. Conway, B. Scott, J. Schirmer, M. Reich, A. Kendl, and the ASDEX Upgrade Team, *Plasma Phys. Control. Fusion* **47**, 1165 (2005).

<sup>22</sup>A. Mlynek, G. Schramm, H. Eixenberger, G. Sips, K. McCormick, M. Zilker, K. Behler, J. Eheberg, and the ASDEX Upgrade Team, *Rev. Sci. Instrum.* **81**, 033507 (2010).

<sup>23</sup>M. Tsalias, N. Tsois, V. Rohde, J. Neuhauser, and the ASDEX Upgrade Team, *J. Nucl. Materials* **337-339**, 751 (2005).

<sup>24</sup>M. Tsalias, D. Coster, C. Fuchs, A. Herrmann, A. Kallenbach, H. W. Mueller, J. Neuhauser, V. Rohde, N. Tsois, and the ASDEX Upgrade Team, *J. Nucl. Materials* **363-365**, 1093 (2007).

<sup>25</sup>M. Tsalias, A. Herrmann, A. Kallenbach, H. W. Müller, J. Neuhauser, V. Rohde, N. Tsois, M. Wischmeier, and the ASDEX Upgrade Team, *Plasma Phys. Control. Fusion* **49**, 857 (2007).

<sup>26</sup>I. H. Hutchinson, *Phys. Plasmas* **15**, 123503 (2008).

<sup>27</sup>I. H. Hutchinson, *Phys. Rev. Lett.* **101**, 035004 (2008).

<sup>28</sup>L. Patacchini and I. H. Hutchinson, *Phys. Rev. E* **80**, 036403 (2009).

- <sup>29</sup>I. H. Hutchinson and L. Patacchini, *Plasma Phys. Control. Fusion* **52**, 124005 (2010).
- <sup>30</sup>S. H. Müller, J. A. Boedo, K. H. Burrell, J. S. deGrassie, R. A. Moyer, D. L. Rudakov, and W. M. Solomon, *Phys. Rev. Lett.* **106**, 115001 (2011).
- <sup>31</sup>S. H. Müller, J. A. Boedo, K. H. Burrell, J. S. deGrassie, R. A. Moyer, D. L. Rudakov, W. M. Solomon, and G. R. Tynan, *Phys. Plasmas* **18**, 072504 (2011).
- <sup>32</sup>S. Potzel, M. Wischmeier, M. Bernert, R. Dux, H. W. Müller, A. Scarabosio, and the ASDEX Upgrade Team, *J. Nucl. Materials* **438**, S285 (2013).
- <sup>33</sup>S. Potzel, M. Wischmeier, M. Bernert, R. Dux, H. W. Müller, A. Scarabosio, and the ASDEX Upgrade Team, *Nucl. Fusion* **54**, 013001 (2014).
- <sup>34</sup>F. Ryter, T. Pütterich, M. Reich, A. Scarabosio, E. Wolfrum, R. Fischer, M. G. Adamov, N. Hicks, B. Kurzan, C. Maggi, R. Neu, V. Rohde, G. Tardini, and the ASDEX Upgrade Team, *Nucl. Fusion* **49**, 062003 (2009).
- <sup>35</sup>P. Sauter, T. Pütterich, F. Ryter, E. Viezzer, E. Wolfrum, G. D. Conway, R. Fischer, B. Kurzan, R. M. McDermott, S. K. Rathgeber, and the ASDEX Upgrade Team, *Nucl. Fusion* **52**, 012001 (2012).
- <sup>36</sup>P. T. Boggs, R. H. Byrd, and R. B. Schnabel, *SIAM J. Sci. and Stat. Comput.* **8**, 1052 (1987).